Microporous and Mesoporous Materials 373 (2024) 113110

Contents lists available at ScienceDirect

Microporous and Mesoporous Materials

journal homepage: www.elsevier.com/locate/micromeso

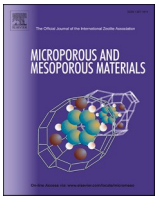

# Microstructure, adsorption site energetics, and formation enthalpy control for FAU-Zeolite $Cs^+$ exchange

Nancy Birkner [a], Vanessa Proust [b,*], Joe Schaeperkoetter [c], An T. Ta [d], Alban Gossard [b], Ayoub Daouli [e], Michael Badawi [f], Nakeshma Cassell [a], Scott Misture [c], Simon R. Phillpot [d], Hans-Conrad zur Loye [g], Kyle S. Brinkman [a], Agnès Grandjean [b]

[a] Department of Materials Science and Engineering, Clemson University, Clemson, SC, 29634-0901, United States
[b] CEA, DES, ISEC, DMRC, Univ Montpellier, Marcoule, France
[c] Kazuo Inamori School of Engineering, Alfred University, Alfred, NY, 14802, United States
[d] Department of Materials Science & Engineering, University of Florida, Gainesville, FL, 32611, United States
[e] Université de Lorraine, CNRS, LPCT, F-54000, Nancy, France
[f] Université de Lorraine, CNRS, L2CM, F-57000, Metz, France
[g] Center for Hierarchical Waste Form Materials and Department of Chemistry and Biochemistry, University of South Carolina, Columbia, SC, 29208, United States

ARTICLE INFO

*Keywords:*
Faujasite
Zeolite microstructure
Cs site-exchange
Thermodynamics
DFT
Calorimetry

ABSTRACT

Cs-137 is a radionuclide fission product that poses a significant risk to life, making it crucial to develop effective methods for its separation and sequestration from nuclear waste streams. Zeolitic structures have emerged as promising materials. This work examines the influence of structure, exchange site energetics, and formation enthalpies of nascent and cation-exchanged Faujasite-X, -Y, and -HY zeolites in terms of their Cs-exchange selectivity. Their interplay was quantified with the application of high-temperature calorimetry, adsorption isotherms, X-ray diffraction and density functional theory (DFT) calculations. Greater efficacy of $Cs^+$ exchange was demonstrated for the $Na^+$-substituted Fau-Y (NaY) zeolite than that of the Fau-X (NaX) and Fau-HY (Na-HY) zeolites. This is explained by a higher amount of $Na^+$ in un-exchangeable sites in the case of NaX and a lower stability in NaY that favors the ionic exchange with $Cs^+$. Moreover, $Cs^+$ incorporation in the structure increases the stability of each kind of zeolite. Correspondingly, structure and DFT analyses demonstrated site-exchange thermodynamic favorability as well as the contribution from cage cell, which resulted in an energy landscape far more conducive to $Cs^+$ incorporation for NaY than either NaX or Na-HY.

## 1. Significance

Application of complementary measurement techniques provide a comprehensive understanding of the underlying mechanisms of Cs exchange capability and capacity in Faujasite zeolites. The insights gained have broad applications from benchmarking quantitative values needed in machine learning in addition to highlight the role of site occupancy effect and thermodynamic stability onto design materials to selective $Cs^+$ removal from nuclear waste streams and environmental remediation strategies.

## 2. Introduction

Cs-137 is the most prolific among the radionuclide fission products. Peril to human, animal, and plant life posed by Cs-137 by accidental or intentional release into the environment cannot be overstated. The gamma emitting radioactive isotope Cs-137 has a 30-year half-life, making it of biological concern in the case of incorporation into vegetation or animals due to the likelihood of being consumed in food [1–3]. With few natural barriers, transport is certain in the natural environment through water, air, and soil [4–9]. With a strong thermodynamic drive to form a fine cesium chloride powder, it travels well by air currents settling elsewhere for continued redistribution. For example, following the Chernobyl, Scandinavian reindeer ~1000 miles away displayed Cs-137 activities well in excess of the recommended safe limits for human consumption in areas where it is a food source [10]. To mitigate the risk of exposure, it is important to develop effective methods for $Cs^+$ separation and sequestration.

* Corresponding author.
*E-mail address:* vanessa.proust@cea.fr (V. Proust).

https://doi.org/10.1016/j.micromeso.2024.113110
Received 8 December 2023; Received in revised form 19 March 2024; Accepted 24 March 2024
Available online 28 March 2024

Nuclear waste form materials are specifically designed to safely contain and immobilize radioactive waste products, ensuring that they do not pose a threat to the environment or public health. These materials are chosen based on their ability to resist leaching, maintain structural integrity under radiation, and chemically bind with the radioactive isotopes. Among the various materials considered for this purpose, zeolites have garnered significant attention due to their unique microporous structures. Zeolites, naturally occurring aluminosilicate minerals, have a high cation exchange capacity, making them particularly effective for immobilizing cesium ($Cs^+$) ions. When compared to other waste form materials, zeolites offer a promising solution for $Cs^+$ ion immobilization due to their stability, abundance, and ability to selectively trap these ions within their framework [11–15].

For example, various processes and inorganic sorbents used to selectively entrap $Cs^+$ from contaminated solution include sodium titanate, silicotitanates, and hexacyanoferrates [16]. However, even the most selective sorbents in saline solution, such as the hexacyanoferrate-based materials, are challenged by an inability to transform easily into a containment matrix with acceptable long-term behavior [17]. One of the most interesting compromises between the cost of the adsorbent, its efficiency, and its shaping in the form of grains for continuous processes is the use of zeolites. Indeed, zeolites were used in the first moments of effluent decontamination at Fukushima [18]. From among the various zeolites, Faujasite (FAU-type) zeolites were chosen for this work, as they provide a typical zeolitic model system for comparison of $Cs^+$ removal efficiency. Typically, Fau-zeolites conform to the general formula $M_{2/n}O{\cdot}Al_2O_3{\cdot}xSiO_2{\cdot}yH_2O$ in which cations (M) have *n* valence, *x* is 2.0 or more, and *y* is the moles of water content in the voids. The FAU-zeolite X or Y corresponds to Si/Al molar ratio lower or higher than two, respectively. Face sharing sodalite cages and d6mr hexagonal prisms are the fundamental building blocks of Faujasites (FAUs) that create a framework conducive to specific sites for ion exchange (Fig. 1).

The negatively charged framework behaves as a Lewis base, neutralized by charge-balancing non-framework alkali and or alkaline metal (M) cations [19]. Because of the Lewis acid-base reaction sites on framework surfaces and internal pores, zeolites intrinsically possess an energetic landscape that may either augment or attenuate adsorption, transport, and sequestration capabilities and tunability-for-purpose [20]. The diffusivity of ions and accessibility of adsorption sites are affected by the zeolite microstructure, such as framework charge balance, pore size, shape, and connectivity, in addition to the interplay of ion- and pore-hydration therein.

Indeed, multiple factors, such as structure, adsorption site energetics, and formation enthalpy (stability) differences, nature of the guest ions, ratio Si to Al, control zeolite $Cs^+$ cation exchange efficiency, phase stability, and immobilization capacity. These factors may collectively act, thereby producing unique energetic landscapes to control the reaction site adsorption characteristics and the kinetic gating of entry to those sites [21,22]. Cage space hydration as well as hydrated ions, although the water may not be strongly surface-bound or strongly coordinated in an ion hydration sphere, can yet dramatically modify local ion properties and surface energetics of the microstructure, which in turn perturb the energy landscape. Ion selectivity is attributed to microstructure reaction sites whose energetic landscapes exert control over ion exchange [23]. Adsorption site energetics, including the adsorption energy and selectivity, determine the exchangeability of cations, such as $Na^+$, $K^+$, and $Cs^+$, to affect the degree of competition for exchange sites and the affinity or selectivity for those ions.

Zeolites are known to exhibit varied performance in $Cs^+$ exchange, influenced by properties such as thermodynamic stability and microstructure [23–26]. However, the factors that control $Cs^+$ exchange selectivity and capacity remain unclear, requiring further investigation. *To that end*, high temperature calorimetry, adsorption isotherms, XRD, and DFT were applied to quantify formation enthalpies, structure, and site-exchange energetics depending on the nature of guest ion (Na+, Cs+, H+) and Si/Al various cation-exchanged Faujasite-X, -Y.

Experimental considerations for the $Cs^+$ exchange reactions include the guest ions, the silica/alumina ratios, and the adsorption site environment and sorption energetics, as well as the hydrating waters within cell cages and about the sorbing cations. The measured contributions of microstructure, exchange site energetics, and formation enthalpies are discussed.

The results of this study will provide insights into the design and optimization of FAU-zeolites for efficient $Cs^+$ removal from nuclear waste and subsequent immobilization.

## 3. Methods

### 3.1. Zeolite preparation, characterization

Two kinds of commercial zeolite powders NaX, NaY and HY (2.6), HY (15) and HY(40) labeled HY-(x) (EnerCat - ALSYS Group) of Faujasite frameworks were selected. The number in the brackets correspond to the Si/Al ratio. To study the role of guest ions ($Na^+$, $Cs^+$) each sample was then saturated by $Na^+$ and $Cs^+$ by mixing commercial zeolites (5 g) with $NaNO_3$ (99.6%, VWR) or $CsNO_3$ (99.99%, Alfa Aesar) rich solution (1 M/50 mL) during 24 at room temperature. Then the powder was washed three times with ultrapure water and dried at 80 °C overnight. These saturated samples are named hereafter $Na^+$-NaX, $Na^+$-NaY, and Na + -HY and $Cs^+$-NaX $Cs^+$-NaY and $Cs^+$-HY. This cation saturation is used to produce a stable reference zeolite. This first step allows to remove impurities and the structure creating a suitable environment stabilized for the ionic exchange mechanism. Chemical compositions of each solid sample were measured after dissolution and analysis by inductively coupled plasma atomic emission spectroscopy, ICP-AES, using a Thermo Scientific iCAP 6000 Series device. Thermogravimetric analysis/differential scanning calorimetry (TGA/DSC) measured water content using the 1 STARe system (Mettler Toledo Instruments) in alumina crucibles. Each sample was heated from ambient temperature to 1000 °C at a rate of 5 °C/min under continuous air as well as $N_2$ flow (30 mL/min and 50 mL/min), respectively. Microstructural pictures were observed by SEM

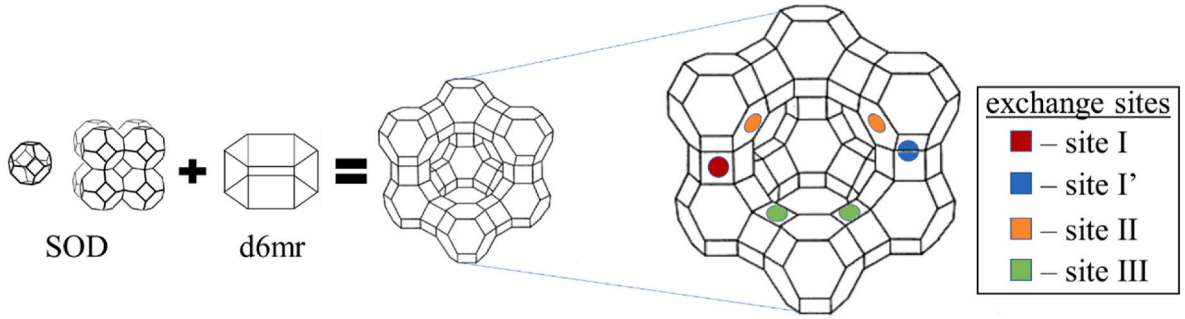


**Fig. 1.** Faujasite building units, Faujasite structure, and possible Faujasite exchange sites within the zeolitic framework.

analysis with scanning Electron Microscopy FEI Inspect S50, high vacuum mode, acceleration voltage of 15 kV, current intensity of 50 nA. Porosity was characterized and quantified using N2 adsorption-desorption isotherms measured at −196 °C using a Quantachrome Novatouch LX3 surface area and pore size analyzer. Prior to analysis, samples were degassed at 90 °C for 24 h. Surface areas were calculated using the Brunauer–Emmett–Teller (BET) method and the volume adsorbed were calculated by BJH method in liquid nitrogen.

### 3.2. $Cs^+$ isotherm sorption measurements

Ion exchange experiment were conducted by contacted 0.02 g (*m*) of powder of NaX, NaY or HY(x) with 10 mL (*V*) of solutions containing various concentration of $CsNO_3$ (from 10 mg/L to 800 mg/L) during 48 h at room temperature. This duration time is enough to reach equilibrium. The atomic adsorption spectrometry (AAS, PerkinElmer AAnalyst 200) was used to determine the $Cs^+$ concentration in the solution before ($[Cs]_i$) and after contact ($[Cs]_f$). Then the sorption capacity at equilibrium ($Q_e$) is given by Eq. 1

$$Q_e = \left([Cs]_i - [Cs]_f\right) m/V \quad \text{Eq. 1}$$

### 3.3. XRD experiments

Structure characterization by X-ray diffraction was carried out on a Bruker D8 advance with Lynxeye XE detector using Cu Kalpha radiation with Kbeta line removed with Ni foil filter. Both Kalpha1 and Kalpha 2 lines were fit with Rietveld refinement of the atomic model using the Topas software. A fundamental parameters approach is used for fitting the line profile and fifth order Chebychev polynomial for background.

### 3.4. High temperature oxide-melt drop solution calorimetry

Zeolite drop solution enthalpies were measured using an AlexSys 1000 (Seteram® Inc.) isoperibol twin-Calvet calorimeter at 800 °C. The binary oxides $Na_2O$, $K_2O$, and $Cs_2O$, $SiO_2$ (cristobalite), and $Al_2O_3$ corundum, being previously unknown at these conditions, were also measured in this work. Calibration of the AlexSys is done using transpose temperature calorimetry against the heat content of corundum as a standard protocol. The calorimeter, the calorimetry method, and the calibration procedure are described in detail elsewhere [27–29]. Very briefly, an experiment involves powdered sample, which is thumb-pressed into pellets subsequently weighed to a mass in the range of 4–6 mg (semi-microbalance). The pellets are dropped at room temperature into platinum crucibles containing 20 g molten sodium molybdate ($3Na_2O{\cdot}4MoO_3$, *abbrev.* NaMo) solvent housed at the bottom of long silica liners seated deep within the calorimeter. In drop solution calorimetry, the dropped oxide sample changes from room temperature to calorimeter temperature and dissolves completely into the molten salt solvent. In general, the total heat effect of drop solution ($\Delta H_{ds}$) includes the heat of solution ($\Delta H_{sln}$) and the heat content of the sample ($\Delta H_T$). Sample-associated water may also evolve as vapor providing an enthalpy contribution that includes the heat content for the phase change as well as that of water-sample adsorption. The calorimeter assemblage is flushed with compressed gas (*approx.* 90 mL/min of oxygen, in this case) which helps maintain a constant gas environment above the melt by removing evolved gases. Additionally, bubbling of gas (*approx.* 5 mL/min of oxygen, here) through the melt controls oxidation state, assists dissolution, and prevents local saturation. Experiments are repeated at least eight times, typically, to achieve statistically reliable data. More specifically to the current experiments, consideration was given to silica dissolution and re-precipitation under the given conditions. Silica-containing samples dissolve and then precipitate as cristobalite [30]. When saturated with silica, subsequent drops do not dissolve, and the heat effect then is equivalent only to the heat content of the final state of the $SiO_2$ (cristobalite). The value of $\Delta H_{ds}(SiO_2)$ strongly depends on silica concentration in the molten solvent. Thus, exceeding the saturation limit of cristobalite in the melt assists in more rapid precipitation of silica from the amorphous or poorly crystalline zeolite samples as they dissolve. To constrain this final state of $SiO_2$ and subsequently use this heat content in a well-defined thermochemical cycle to compute the heat of formation of the amorphous zeolite samples, 50 mg amorphous silica ($SiO_2$, Alfa Aesar, 99.9% metals basis) was added prior to drop solution measurements. The measured mean drop-solution enthalpies compute the enthalpy of formation reactions from the binary oxides ($Al_2O_3$, $Na_2O$, $K_2O$, $Cs_2O$, $SiO_2$, and $H_2O$ in the present work) and the standard heats of formation from the elements at 25 °C through the application of stoichiometrically appropriate thermochemical cycles.

### 3.5. Density functional theory calculations and structure modeling

Periodic density functional theory (DFT) calculations were performed using the Vienna *Ab Initio* Simulation Package (VASP) [31–33]. The Kohn-Sham equations were solved self-consistently until energies reached an accuracy of $10^{-6}$ eV. Atomic positions were fully relaxed until forces were smaller than 0.02 eV/Å per atom. Chemical behaviors were modeled using the generalized gradient approximation (GGA), Perdew-Burke-Ernzehof (PBE) exchange correlation functionals [34] and the Projector Augmented Wave (PAW) [35,36] method. The inner-core *s* and *p* electrons were also treated as valence states for the $Cs^+$ and Na $^+$ atomic species while standard valence potentials were used for Al, O, Si, and H atoms when applicable. A plane-wave cutoff energy of 700 eV was used and systems were sampled using a 1 × 1 × 1 Monkhorst-Pack *k*-point grid [37]. To better describe long-range interactions the DFT-D2 Grimme dispersion correction method was also used [38].

Computational cost was reduced by using a rhombohedral cell of 144 atoms [39–41] (Fig. 2) with the chemical formula $Na_{20}Al_{20}Si_{28}O_{96}$ and $Na_{14}Al_{14}Si_{34}O_{96}$ for the X and Y zeolite, respectively. The adsorbed ion positions in these models were based on previous experimental/computational works [41–43]. Single site exchanged models were created by replacing one $Na^+$ ion with one $Cs^+$ at a respective site in the Na-X and Na–Y models.

To account for solvation effects, relevant ion exchange sites in X/Y systems were *micro solvated* with 4–5 water molecules to compensate for any coordination deficit experienced by adsorbed $Cs^+$. All other exchange sites in the super cage that were occupied by $Na^+$ were also solvated with two water molecules to mitigate water desorption from the $Na^+/Cs^+$ exchange site of interest. Fig. 2 shows the micro solvated model for NaY, while visual depictions of the other zeolite models can be found in Supporting Information.

To better resolve the atomistic picture of the $Cs^+$ exchanged NaX and NaY zeolites, the following exchange reactions were modeled using DFT calculations,

$$Na_nX \bullet 33H_2O + Cs(H_2O)_{10}^+ \rightarrow CsNa_{n-1}X \bullet 33H_2O + Na(H_2O)_4^+ + 6H_2O \quad \text{Eq. 2}$$

$$Na_nY \bullet 38H_2O + Cs(H_2O)_{10}^+ \rightarrow CsNa_{n-1}Y \bullet 38H_2O + Na(H_2O)_4^+ + 6H_2O \quad \text{Eq. 3}$$

Based on these processes, the exchange energies at different sites can be determined with the following equations,

$$E_{exch,X} = E_{Na(H_2O)_4^+} + E_{CsNa_{n-1}X\bullet 33H_2O} + 6E_{H_2O} - E_{Cs(H_2O)_{10}^+} - E_{Na_nX\bullet 33H_2O} \quad \text{Eq.4}$$

$$E_{exch,Y} = E_{Na(H_2O)_4^+} + E_{CsNa_{n-1}Y\bullet 38H_2O} + 6E_{H_2O} - E_{Cs(H_2O)_{10}^+} - E_{Na_nY\bullet 38H_2O} \quad \text{Eq.5}$$

where $E_{Na(H_2O)_4^+}$ is the energy of $Na(H_2O)_4^+$ molecule, $E_{Cs(H_2O)_{10}^+}$ is the energy of $Cs(H_2O)_{10}^+$ molecule, $E_{H_2O}$ is the energy of a water molecule in the bulk, $E_{CsNa_{n-1}X\bullet 33H_2O}$ is the energy of a single $Cs^+$ exchanged Na-X,

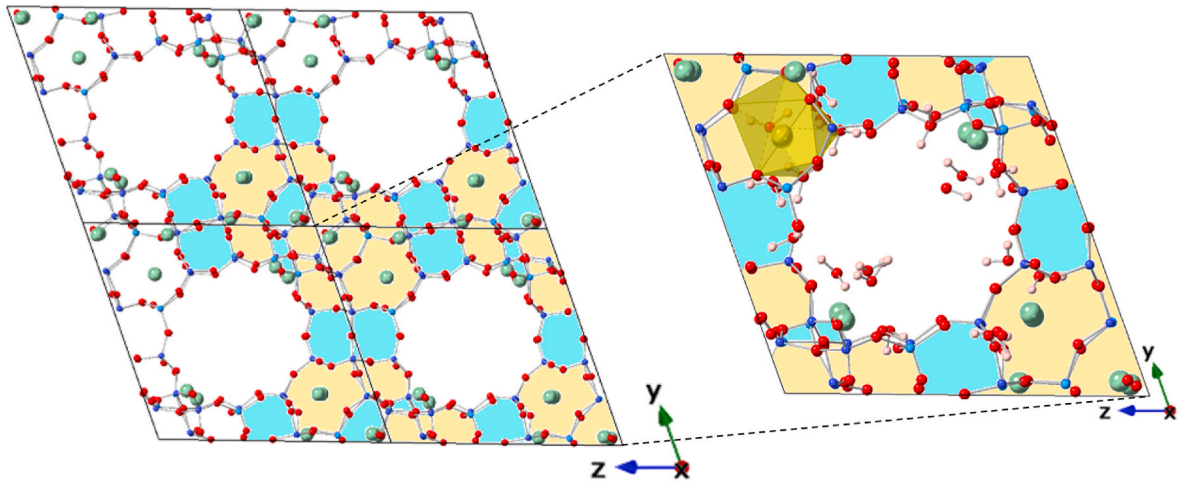


**Fig. 2.** Supercell of bare $Na_nY$ (left) and primitive cell of micro-solvated $Na_nY \bullet 38H_2O$ (right). For clarity, system cell boundaries are denoted with solid lines and some sodalite and d6mr units are shaded in yellow and blue, respectively. Al atoms are shown in cyan, Si in blue, O in red, and Na in green. The site II used for $Cs^+$ exchange is highlighted with a yellow polyhedron.

$E_{Na_nX\bullet 33H_2O}$ is the energy of Na-X zeolite, $E_{CsNa_{n-1}Y\bullet 38H_2O}$ is the energy of a single $Cs^+$ exchanged Na–Y, and $E_{Na_nY\bullet 38H_2O}$ is the energy of Na–Y zeolite.

The free pore volumes of the bare X and Y models (i.e., no water present) were also calculated using the Zeo++ software package [42] to gain deeper insight on the zeolite structure. The calculations were conducted with a probe molecule of 0.0 Å to accurately determine the pore volume.

**Table 1**
$Na^+/Cs^+$-saturated zeolite samples identification, molar composition from ICP-MS and TGA, water content (wt %), Si-to-Al ratio in the molecular formula, guest ion content (M/Si ratio); Specific surface area ($S_{BET}$), microporous surface ($S_M$) and total pore volume ($V_M$), measured using nitrogen adsorption/desorption and analyzed using the t-plot method; mean drop solution enthalpy as measured at 804 °C in sodium molybdate for hydrous ($\Delta H_{ds}$) and anhydrous ($\Delta H_{ds\text{-}corr}$) zeolites, and the enthalpy of formation from the component binary oxides ($\Delta H_{f,ox}$) at 25 °C.

| Sample ID | Molecular Formula (ICP-MS, TGA) | Wt.% $H_2O$ | Si/Al | M/Si | $S_{BET}$ $m^2$/mmol | $S_M$ $m^2$/mmol | $V_M$ $cm^3$/mol | Mean $\Delta H_{ds}$[a] (kJ/mol) | $\Delta H_{ds\text{-}corr}$[b,†] (kJ/mol) | $\Delta H_{f,ox}$ (kJ/mol) |
|---|---|---|---|---|---|---|---|---|---|---|
| NaX | $H_{0.1}K_{0.1}Na_{0.3}Si_1Al_{0.5}O_4{\cdot}1.1H_2O$ | 15 | 2 | 0.5 | 59.9 | 52.5 | 27.4 | 255.39 ± 5.13 | 174.85 ± 5.85 | −142.42 ± 6.78 |
| NaY | $H_{0.1}$ $K_{0.002}Na_{0.2}Si_1Al_{0.3}O_3{\cdot}0.98H_2O$ | 17 | 3.1 | 0.3 | 63.2 | 60.4 | 31.2 | 214.60 ± 3.77 | 142.84 ± 4.49 | −97.56 ± 5.82 |
| $Na^+$-NaX | $H_{0.01}K_{0.09}Na_{0.5}Si_1Al_{0.6}O_4{\cdot}2H_2O$ | 23 | 1.6 | 0.6 | | | | 322.90 ± 5.93 | 176.46 ± 6.65 | −156.47 ± 7.42 |
| $Cs^+$-NaX | $H_{0.1}Cs_{0.4}K_{0.1}Na_{0.4}Si_1Al_{0.9}O_4{\cdot}1.3H_2O$ | 11 | 1.1 | 0.9 | 58.1 | 47.9 | 24.7 | 332.61 ± 6.45 | 237.43 ± 7.17 | −272.02 ± 8.01 |
| $Na^+$-NaY | $H_{0.1}$ $K_{0.001}Na_{0.2}Si_1Al_{0.3}O_3{\cdot}1.7H_2O$ | 25 | 3.1 | 0.3 | | | | 253.25 ± 4.46 | 128.77 ± 5.18 | −77.90 ± 6.31 |
| $Cs^+$-NaY | $H_{0.1}Cs_{0.2}Na_{0.06}Si_1Al_{0.4}O_3{\cdot}1.2H_2O$ | 16 | 2.5 | 0.36 | 60.1 | 52.9 | 27.2 | 222.90 ± 4.88 | 135.03 ± 5.60 | −104.01 ± 6.81 |
| $Na^+$-HY (2.6) | $H_{0.3}K_{0.0002}Na_{0.002}Si_1Al_{0.3}O_3{\cdot}0.7H_2O$ | 13 | 3.3 | 0.3 | | | | 153.42 ± 2.74 | 102.17 ± 3.46 | −37.50 ± 5.24 |
| $Cs^+$-HY (2.6) | $H_{0.36}Cs_{0.03}Na_{0.01}Si_1Al_{0.4}O_3{\cdot}0.7H_2O$ | 12 | 2.5 | 0.4 | 46.9 | 37.5 | 19.7 | 153.55 ± 1.63 | 102.30 ± 2.35 | −37.94 ± 5.01 |
| $Na^+$-HY (15) | $H_{0.009}K_{0.0001}Na_{0.0007}Si_1Al_{0.05}O_2{\cdot}0.7H_2O$ | 14 | 18 | | | | | | | |
| $Cs^+$-HY (15) | $H_{0.04}Cs_{0.04}Si_1Al_{0.08}O_3{\cdot}0.5H_2O$ | 13 | 13 | 0.08 | 56.9 | 44.9 | 23.1 | | | |
| $Na^+$-HY (40) | $H_{0.003}K_{0.0002}Na_{0.002}Si_1Al_{0.024}O_2{\cdot}0.07H_2O$ | 0.4 | 42 | 0.0024 | | | | | | |
| $Cs^+$-HY (40) | $H_{0.016}Cs_{0.009}Si_1Al_{0.025}O_2$ | | 40 | 0.025 | 34.7 | 27.7 | 14.4 | | | |
| HY (2.6) | $H_{0.3}K_{0.003}Na_{0.005}Si_1Al_{0.4}O_3{\cdot}0.6H_2O$ | 11 | 2.5 | 0.4 | 42.5 | 37.3 | 19.6 | 149.08 ± 2.81 | 105.15 ± 3.53 | −33.53 ± 5.25 |
| HY (15) | $H_{0.06}Na_{0.006}Si_1Al_{0.06}O_{2.13}{\cdot}0.4H_2O$ | 10 | 16 | 0.06 | 47.2 | 38.1 | 19.2 | 102.79 ± 1.84 | 73.50 ± 1.94 | −22.26 ± 4.78 |
| HY (40) | $Na_{0.03}Si_1Al_{0.024}O_{2.06}$ | 0 | 41 | 0.24 | 37.2 | 31.3 | 14.5 | 50.36 ± 0.71 | 50.36 ± 0.71 | −5.01 ± 4.47 |

[an] Enthalpy of drop solution for the hydrous sample ($\Delta H_{ds}$) and.

[b] That corrected ($\Delta H_{ds\text{-}corr}$) for bulk water content (anhydrous form of the sample) are the measurement mean with the uncertainty computed to a two-standard deviation. The errors reported for the enthalpy of formation from the binary oxides ($\Delta H_{f,ox}$) are propagated errors computed as the square root of the sum of the squares of measurement uncertainties.

## 4. Results and discussion

### 4.1. Composition

Cation adsorption by zeolites is influenced by the chemical species, the concentration of competitive cations in aqueous phase, the pH, and the zeolitic framework through their maximum cation exchange capacity (CEC). The CEC of zeolites has been assumed to be equivalent to the amount of negative surface charge due to the trivalent Al (Fig. 1). CEC values of 4.40 mmol $g^{-1}$ in NaX and 2.40 mmol $g^{-1}$ in NaY in alkaline media (pH from 8 to 10) are reported in the literature [43]. However, recent works highlight the influence of the pH on zeolite's CEC showing a decrease with the decreasing pH even from neutral to alkaline region.

In this study, rather than calculate CEC in mmol.$g^{-1}$ for each sample, that leads difficulty to compare data due to the fact each guest ion has not the same molecular mass, we propose to evaluate the exchangeability by the content of all cations contained in the structure in mmol/mol (equal to the amount of negative charge), i.e. $K^+$, $H^+$, and $Na^+$ for $Na^+$- zeolites. The comparison of this amount by all the cations contained in $Cs^+$- zeolites will give us information about the modification of the structure by incorporation $Cs^+$ as guest ion, and the same for acidic zeolite. So we use here the ratio M/Si (with $M = K^+ + H^+ + Na^+ + Cs^+$) as indicator of the amount of guest ions sites. These values are obtained using the chemical formula in Table 1 and reported in the same table. Fig. 3 reports also the ratio (%) of each guest ion (relative to the total amount of guest ion) in the structure for all samples.

The amount of guest ions per silicon atom of $Na^+$-NaX is near 0.6 to compare to 0.3 for $Na^+$-NaY and for $Na^+$-HY. The other acidic zeolite with low alumina content show very low guest ions inside the structure, and then exchangeable sites, in agreement with the low amount of Al. These values conform to the literature for a same pH [44]. The decrease of the Si/Al seems to be correlated to the slightly lower pH of the Cs solution inducing an acidity media favorable to dealumination phenomena and defects in the zeolite structure.

*These results tend to conclude a higher sorption capacity for $Na^+$-NaX compare to $Na^+$-NaY and $Na^+$-HY 2.6, and a very low sorption capacity for the other two acidic zeolites.*

The amount of guest ions per silicon atom increases from 0.6 to 1 for $Na^+$-NaX to $Cs^+$-NaX respectively. The insertion of $Cs^+$ in the structure does not change the amount of guest ions for NaY (close to 0.3 for both $Na^+$-NaY and $Cs^+$-NaY) and also for HY(15) (close to 0.1 for both $Na^+$-HY(15) and $Cs^+$-HY(15)). *This tends to show that the FAU-X is more affected by the insertion of $Cs^+$ inside the structure.* This is consistent to the fact that there is a strong variation of the Si/Al ratio by replacing $Na^+$ by $Cs^+$ in FAU-X, from respectively 1.6 to 1.1, which is not the case in FAU-Y with the Si/Al ratio close to 3.

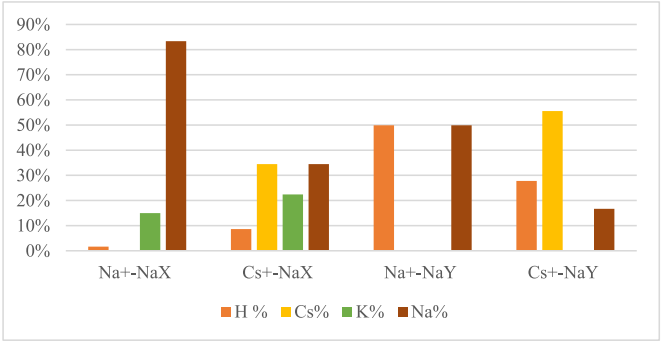


**Fig. 3.** Repartition of guest cation (%) in the structure of each zeolite studied ($Na^+$-NaX, $Cs^+$-NaX, $Na^+$-NaY and $Cs^+$-NaY) from the composition given in Table 1.

### 4.2. Porosity

The $N_2$ adsorption/desorption isotherms of nascent zeolite and $Cs^+$ saturated zeolite are shown in Fig. 4. $Na^+$-saturated zeolite cannot be analyzed by this method due to no observed $N_2$ adsorption. This phenomenon can be explained by the presence of $Na^+$ near to the pore opening avoiding totally or partially the nitrogen molecules access to the microporosity [45,46]. The polarity phenomenon can also be take into account causing hydrophilicity/hydrophobicity and electrostatics effects. The heterogeneous $N_2$ adsorption can be influenced by the polarization mainly due to electric field-quadrupole moment interactions, the distribution and size of cations contained in the zeolitic structure [47].

Total pore volume and specific surfaces area (BET and microporous) are reported in Table 1 (these data are given in $cm^3$/mol and $m^2$/mmol to take into account the variation of molar mass of the samples). Nascent zeolite particles are primarily microporous with a varying 0.2–0.3 $cm^3$ $g^{-1}$ total pore volume (around 30 $cm^3$/mol) and 400–800 $m^2$/g BET specific surface area (around 60 $m^2$/mmol) and a small mesopore volume that can be attributed to interparticle volume. The presence of a hysteresis loop in the $N_2$ adsorption/desorption isotherm of HY with a closure point at $P/P_0 = 0.47$ also supports the presence of an internal cavity. Mesopores, connected to the exterior by apertures, are often found within aggregated crystals of zeolites and some mesoporous zeolites. Here aggregation can be observed on SEM pictures in Fig. 5.

$Cs^+$-saturated zeolites show a significant decrease of microporous surfaces area and volumes, and only a small decrease of the BET surface area. These measured losses of porosity could be attributed to the presence of $Cs^+$ species inside the zeolite cavities.

### 4.3. Exchange site location and energetics

Geometric changes affected by the Si/Al ratio and acid-bases site seem playing a key role on the framework exchange site. The hydrated materials can be generally represented by formula $M^+_x[(AlO_2)_x(SiO_2)_y]\cdot wH_2O$, where the acid–base sites are related to the different charge of $Al^{3+}$ and $Si^{4+}$ and $Na^+$ or $H^+$ ensure the electroneutrality to both framework and extra-framework. Variations in Si/Al ratio result on different electronic charge distribution and having lower Si/Al ratio provides more Si–O–Al than Si–O–Si bonds, and consequently more negative charge sites and more interactions with cations coming from the tetrahedral Al of the crystal lattice (the only configuration confirmed by MAS NMR of $^{27}Al$ as predicted).

As shown on Fig. 6, $Cs^+$-NaX (Si/Al~1) showed a lower rate of $Cs^+$ compared to the total available adsorption site rate with 40 %–56 % for $Cs^+$-NaY (Si/Al~2.5) although the faujasite-type structure is similar. *This indicates that, in the NaX, some Na + ions are less exchangeable with $Cs^+$ than in NaY.* Moreover, in NaX the negative charge are partly compensated by the adsorption of $H^+$ from the media in competition with $Cs^+$. This hypothesis is confirmed by the repartition of guest cation shown on Fig. 6. As these exchange reactions occur into the cages of the structure, the zeolite shape selectivity and the steric effect of the $Cs^+$ adsorption must also be taken into account.

The exchangeability of $Na^+$ and $Cs^+$ at the different charge balancing sites was monitored with PXRD. XRD scans were collected for the Faujasites after ionic exchange with $Na^+$and $Cs^+$. The complete atomic structure results from Rietveld refinement are tabulated in Supplementary Tables S2–S7 with the resulting bond distance calculations for extra-framework cations tabulated in Supplementary Table S8 and S9. A summary of the atomic structure results are tabulated in Table 2.

The model of Lee et al. [48] was used to initiate refinements of the NaX parent structure with space group $Fd\bar{3}^{''-}$ Of the 16 hexagonal prisms per unit cell in faujasite, 14 were found to be occupied by Na sitting at Site I, leaving on average 2 hexagonal prisms unoccupied in the parent NaX structure. The 5 Na atoms sitting at site I′ presumably occupy the 4 hexagonal windows where site I is vacant. It was found that Na at

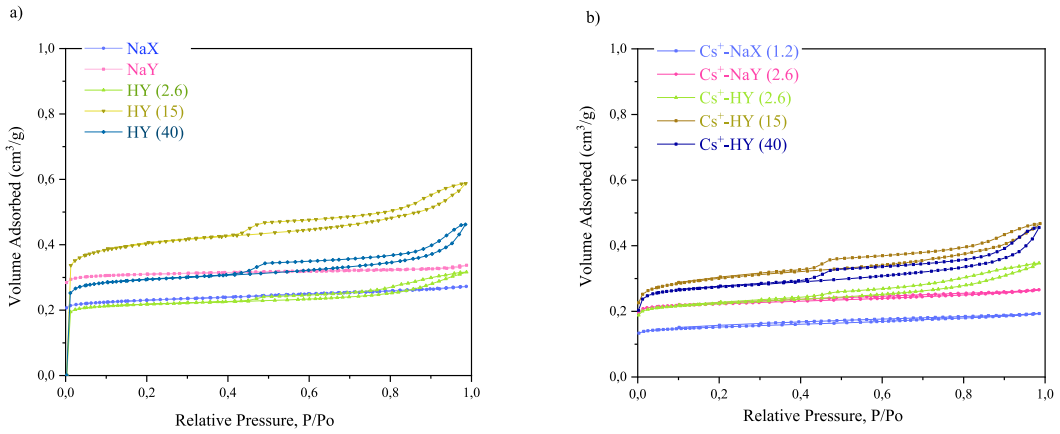


**Fig. 4.** Nitrogen adsorption/desorption isotherms of nascent sodium zeolite and acid zeolite samples a) and $Cs^+$-saturated zeolite b).

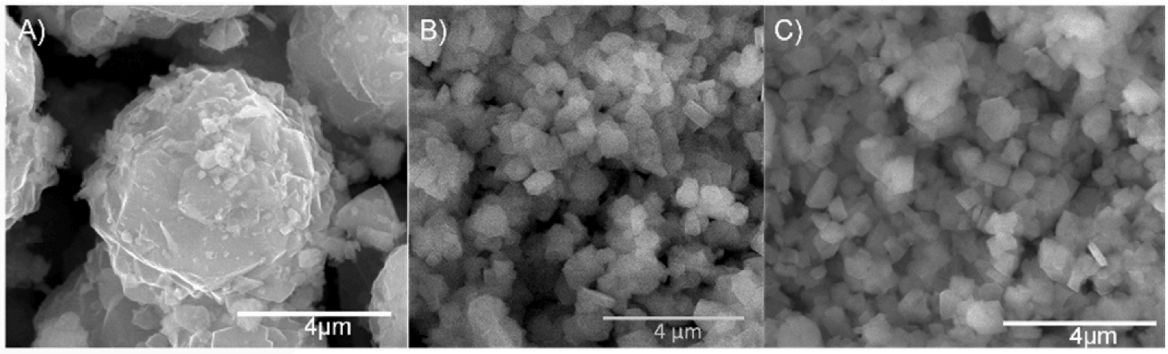


**Fig. 5.** SEM micrographs that correspond to (A) NaX, (B) NaY, and (C) HY zeolite.

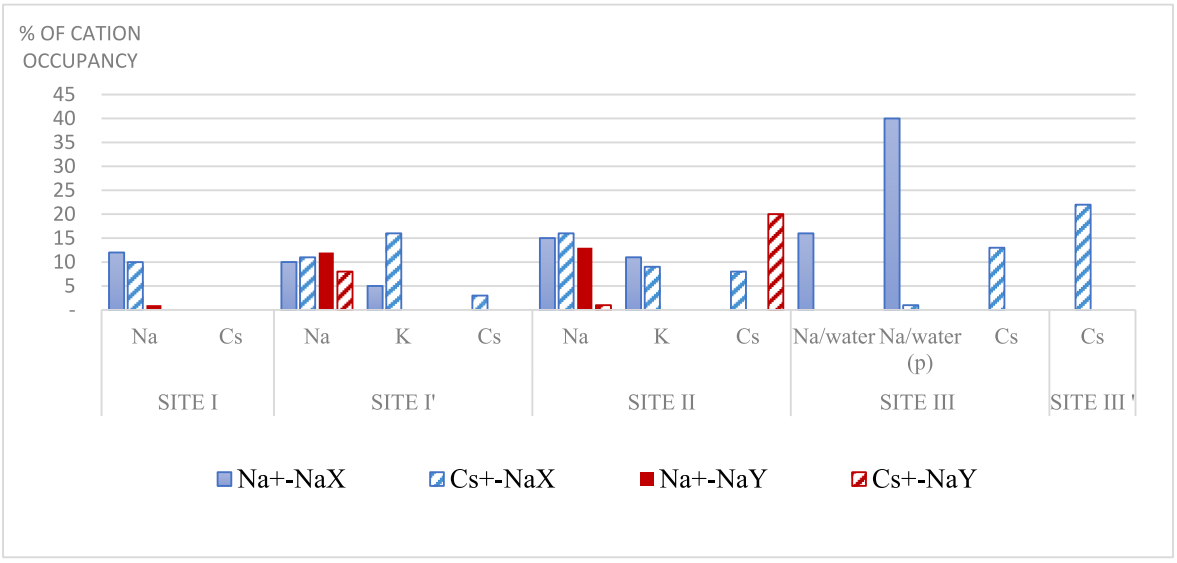


**Fig. 6.** Occupancy of each cation in the various site of zeolite.

site I′ tends to sit directly in the center of the hexagonal window between hexagonal prism and the sodalite cage whereas K tended to migrate further into the sodalite cage. This migration of K at site I′ into the sodalite cage allows the simultaneous occupation of Na at Site I with K at site I′ which has been reported for several K-containing zeolites [48,49]. Some of the electron density at either site I or site I′ attributed to Na may be from water which explains why the total population of Na at sites I and I′ does not obey the relation nSI + nSI' ≤ 16. Only 15 of the 32 total site I′ positions are occupied on average which may suggest that K atom is found at site I′ on only one side or the other of the hexagonal prism with an associated minor displacement of Na at site I in the opposite direction. The total occupancy of Na and K at site II is found to be 25 of

**Table 2**
NaX and NaY series extra-framework cation site occupancies per unit cell.

| Site | NaX | Na-NaX | Cs-NaX | NaY | Na–NaY | Cs–NaY |
|---|---|---|---|---|---|---|
| Na–I | 14 | 12 | 10 | 1 | 1 | 0 |
| Na–I′ | 5 | 10 | 11 | 12 | 12 | 8 |
| K–I′ | 10 | 5 | | | | |
| Na-II | 15 | 15 | 16 | 13 | 12 | 1 |
| K-II | 10 | 11 | 9 | | | |
| Na-III/water | 14 | 16 | | | | |
| NaI-IIp/water | 36 | 40 | | | | |
| Cs–I′ | | | 3 | | | |
| Cs-II | | | 8 | | | 20 |
| Cs-III | | | 13 | | | 0 |
| Cs-III’ | | | 22 | | | 0 |
| water | 252 | 254 | 181 | | | 279 |

**Table 3**
Results from Rietveld refinement of atomic models to XRD data.

| Sample | Lattice Parameter (Å) | Site I Occ | Site I′ Occ | Site II Occ | Site III Occ |
|---|---|---|---|---|---|
| | | $N_p = 16$ | $N_p = 32$ | $N_p = 32$ | $N_p = 48$ |
| NaX | 25.01261(6) | Na: 0.98 (02) K: 0 | Na: 0.42(4) K: 0.16(2) | Na: 0.35(5) K: 0.46(3) | Na: 0.29 |
| $Na^+$-NaX | 25.0272(5) | Na: 0.80 (2) K: 0 | Na: 0.17(3) K: 0.18(2) | Na: 0.81(2) K: 0.09(1) | Na: 0.33 |
| $Cs^+$-NaX | 25.0111(4) | Na: 0.84 (2) K: 0 Cs: 0 | Na: 0.36(1) K: 0.09(1) Cs: 0 | Na: 0.37(1) K: 0.06(1) Cs: 0.27(1) | Cs: 0.43 (1) |
| NaY | 24.6503(6) | Na: 0.15 (2) | Na: 0.37(1) | Na: 0.33(1) | 0 |
| $Na^+$-NaY | 24.6493(4) | Na: 0.10 (2) | Na: 0.36(1) | Na: 0.32(1) | 0 |
| $Cs^+$-NaY | 24.6616(7) | Na: 0.01 (2) Cs: 0 | Na: 0.01(5) Cs: 0.06(2) | Na: 0.09(1) Cs: 0.56(2) | Cs: 0.01 (1) |

Occupancy was abbreviated to “Occ”. The exchange sites are listed in the header row with the multiplicity of each site (per unit cell) denoted as $N_p$. The occupancy of each site by the labeled cations is tabulated in the following rows with uncertainty in the last digit specified in parentheses.

the 32 total sites per unit cell. The migration of K at site I′ into the sodalite cage may limit the total occupancy of Site II, which is also located in the sodalite cage. Unambiguous assignment of the electron density at Site III and III’ is difficult due to the presence of water in the supercage with an associated disorder in the position [41]. We have followed the example of Lee et al. by assigning the atomic density to a combination of water and sodium. The resulting large thermal parameters and relatively long Na–O bond distance for this site (~2.9 Å) reflect the significant disorder at the site. After Na ion exchange with the parent NaX, we see a decrease in K at site I′, which is still displaced slightly into the sodalite cage but less so than in the parent structure. The decrease of K at site I′ is accompanied by an increase in the Na at site I′ and a slight loss of Na of Site I in accordance with the conditions of simultaneous occupancy of Na at site I and I’. Subsequent ion exchange with $CsNO_3$ leads to Cs now at site II and III/III’. Because of the significantly different arrangement of solvated water with Cs sitting at Site III a different starting model was used for refinement of water positions and occupancies along with the associated cations [50]. Cs at site II is accompanied by decreases in K at both site I′ to accommodate the larger Cs atom in the sodalite cage. We find that nearly all the Na at site III/III’ has been replaced with Cs but Na and K at sites I, I’ and II are resistant to fully exchange.

The model of Arletti et al. [51] was used to initiate the refinements on the NaY parent structure. In the case of NaY only 1 of the 16 hexagonal prisms is occupied on average by Na. Site I′ and II are both occupied, with around 12 Na atoms per unit cell at each site. The relative occupancies remain effectively unchanged after Na ion exchange as the parent structure was already charge balanced exclusively with Na. After Cs ion exchange, though, approximately 65% of the crystallographically discernible Na ions are replaced with Cs ions, with 20 Cs ions occupying site II. Only site I’ retains Na ions with approximately 8 per unit cell found there.

For the aluminum tetrahedra, the parent structure of NaX has charge-balancing $Na^+$ and $K^+$ ions whereas that of NaY has only $Na^+$ ions. Steric hindrance plays a significant role in how the exchange sites are populated. As shown in Table 3, Site I is the least accessible site both nascent parents X- and Y-FAU. Both lose $Na^+$ content during the $Na^+$ exchange process (18% and 33%, respectively) although NaX begins with 85% greater Na-ion content than Na–Y. As shown in Fig. 6 and Table 3, with Cs-saturated in the Cs-NaX, $Na^+$ content in site I is 4.8% higher than for Na saturated Na-NaX zeolite whereas, conversely, Na + amount in site decreased significantly in Cs–NaY by 90% compared to Na–NaY. However, that 4.8% is very small and is within the error meaning.

$Cs^+$, with a larger ionic radius, is only exchanged at the more accessible site II. Importantly, Fau-X has a higher percentage of $Na^+$ ion that occupy sites I and I′ in the $Cs^+$-NaX saturated product. In this case, for Site I, this means 13 of the total 16 sites are populated by $Na^+$ while there are zero sites being occupied by $Cs^+$. For example, $Cs^+$-NaX has 84% of its $N_p$ “site population” occupied by $Na^+$ versus zero $Cs^+$ ions. For Site I′ in $Cs^+$-NaX, 11–12 sites (36%) out of a total of 32 are associated with $Na^+$ while $Cs^+$ occupies not one of these sites. This suggests hindrance of $Cs^+$ exchange at Site I′, despite the much greater total number of exchangeable $Na^+$ cations in the NaX structure. Likewise for Fau-Y, which possesses similar abundant Site I’ population ($N_p = 32$) as that of the NaX process, also $Cs^+$ did not appreciably exchange at these sites (0.06%, 1–2 sites). Moreover, as shown in Table 1, during the $Cs^+$ exchange process, the total amount of $Na^+$ was lost from the NaY structure, unlike the NaX structure in which $Na^+$ was nearly doubled. For NaX, $Cs^+$ exchange occurred at 27% (8–9 sites) of Site II positions. Conversely, for NaY, Site II demonstrated the greater percentage of $Cs^+$ exchange (56%) with 18 sites out of the total 32 Site II positions occupied in $Cs^+$-NaY.

The $Cs^+$ exchange energies at sites II and III for Na-X and site II for Na–Y were calculated using DFT. Notably, site I and I’ exchanges were not considered since our experimental findings as well as previous reports [41] have shown that such exchanges do not occur readily. Overall, $Cs^+$ exchange is the most favorable in Na-X at site III ($E_{exch,X} = -1.815$ eV) followed by Na-X at site II ($E_{exch,X} = -1.615$ eV) and the least favorable being exchange in Na–Y site II ($E_{exch,Y} = -0.775$ eV). Using Zeo++ software [42], the Na-X zeolite was found to have a smaller accessible pore volume (0.328 $cm^3/g$) than the Na–Y zeolite (0.367 $cm^3/g$). The thermodynamic predictions help explain the XRD characterization reported in Table 3 when comparing the relative exchange favorability between X/Y zeolites and sites III/II in Na-X. Furthermore, our computational work also suggests that the larger accessible pore volume in NaY can also be a contributing factor to the overall $Cs^+$ adsorption capacity in Na–Y.

These analysis and calculation confirm that NaX exhibits higher amount of un-exchangeable Na+, located in Site I and Site I’, than NaY. By contrast, NaY allows a better insertion of $Cs^+$ in the structure by filling site III. *This does not support the conclusion drawn from the observations of the guest ion content in the structure, that NaX with higher guest ions could incorporate more Cs than NaY. Indeed, the nature of the site occupied by the guest must be taken into account. According to this, NaX should show lower Cs* $^+$ *exchange capacity than NaY.*

### 4.4. Calorimetry

Formation enthalpies of the zeolites were obtained from mean drop solution enthalpy ($\Delta H_{ds}$) values. Samples were measured in sodium molybdate ($3Na_2O{\cdot}4MoO_3$, *abbrev.* NaMo) solvent at 804 °C with an AlexSys 1000 (Seteram® Inc.) isoperibol Calvet twin calorimeter, which is housed at Clemson University. Using drop solution enthalpy data of

the samples along with their binary oxide ($Al_2O_3$, $H_2O$, $K_2O$, $Na_2O$, $SiO_2$) formation reactants in their correct stoichiometry, the appropriate thermochemical cycles (Table 3) were applied to compute the enthalpy of formation from the oxides ($\Delta H_{f,ox}$) at 25 °C for the samples. Additionally, the thermochemical cycles account for stoichiometric water content by adding the applicable enthalpy of water for the sample (bulk level versus chemically bound) and the heat content correction for the temperature and phase change from room-to-calorimeter temperature. TGA-DSC measurements indicated that the water associated with the zeolites (Table 1,Figure S1 a-c) was removed up to 300 °C, which corresponds as physisorbed or bulk-level hydration. Thus, the TGA-DSC results suggest that the energetics of water adsorption on these zeolites have an integral enthalpy like that of water condensation under standard state conditions. Table 4 summarizes the thermochemical cycles and applicable enthalpies of reactant binary oxides and the measured enthalpies of the nascent FAU-zeolite samples and their Na- and Cs-exchanged products. Plots of their corresponding stability relationships are shown in **Figure** Further details of the applied thermochemistry methods, calculations, and results are found in the Supporting Information in Tables S10 and S11.

### 4.5. Solution enthalpies

Although not a rule, as systems vary in chemical complexity, increased ease of dissolution into the melt generally corresponds to a less positive enthalpy of solution and a decrease in condensed phase stability. In the zeolite samples, the mean enthalpy of drop solution ($\Delta H_{ds}$) tracks inversely with Si/Al (Table 1 and Fig. 7). Enthalpies of solution become more exothermic (easier to dissolve) as Si/Al increases, for instance, 255.39 ± 5.13 (NaX) > 214.60 ± 3.77 (NaY) > 149.08 ± 2.81 (HY 2.6) > 102.79 ± 1.84 (HY 15) > 50.36 ± 0.71 (HY 40) in units kJ/mol. The $\Delta H_{ds}$ trends for the $Na^+$- and $Cs^+$-exchanged zeolites, respectively, follow as 322.90 ± 5.93 ($Na^+$-NaX) > 253.25 ± 4.46 ($Na^+$-NaY) > 153.42 ± 2.74 ($Na^+$-HY) and 332.61 ± 6.45 ($Cs^+$-NaX) > 222.90 ± 4.88 ($Cs^+$-NaY) > 153.55 ± 1.63 ($Cs^+$-HY) in units kJ/mol. The energetic trends of *decreasing stability with increasing* Si/Al correspond with previous reports. Solution enthalpies of amorphous and nanoparticle silica and their rates of dissolution have been recognized as correlating with silicate molecular structure [52]. *Enthalpies and rates of dissolution increase* (more readily dissolved and thus *less stable*) *with increased organization of* the silica structure. Conversely, as aluminum content increases (decreased Si/Al ratio), *solution enthalpies* become more energetically stable (shifting endothermically for the dissolution enthalpy, and hence more stable), reaching a maximum near x = Al/(Al + Si) (0.5) [53].

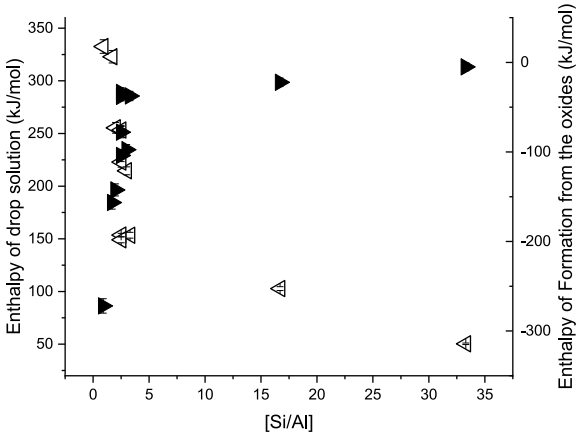


**Fig. 7.** Mean enthalpy of drop solution (left axis, left-facing solid arrows) and enthalpy of formation from the binary oxides at 25 °C (right axis, right-facing solid arrows) are plotted against the Si/Al ratio.

**Table 4**
Thermochemical cycles that computed zeolite sample formation enthalpy from the binary oxides ($\Delta H_{f,ox}$) at 25 °C using the stoichiometry of the samples.

| Formation enthalpy from the binary oxides ($\Delta H_{f,ox}$) at 25 °C | Mean $\Delta H_{ds}$ (kJ/mol) |
|---|---|
| $[K_{(0.5x)}Na_{(0.5y)}Cs_{(0.5z)}Al_{(0.5m)}Si_{(1.0)}O_{(q(0.5(x+y+z+m)+Si)}.nH_2O]_{(s,\ 25\ °C)} \rightarrow [(½)\{xK_2O + yNa_2O + zCs_2O + mAl_2O_3\} + SiO_2]_{(sln,\ 804\ °C)} + nH_2O_{(g,\ 804\ °C)}$ | $\Delta H_1 = \Delta H_{ds}$(sample)† |
| $K_2O_{(s,\ 25\ °C)} \rightarrow K_2O_{(sln,\ 804\ °C)}$ | $\Delta H_2$ ($K_2O$) = −287.60 ± 3.33† |
| $Na_2O_{(s,\ 25\ °C)} \rightarrow Na_2O_{(sln,\ 804\ °C)}$ | $\Delta H_3$ ($Na_2O$) = −193.27 ± 1.69† |
| $Cs_2O_{(s,\ 25\ °C)} \rightarrow Cs_2O_{(sln,\ 804\ °C)}$ | $\Delta H_4$ ($Cs_2O$) = −335.20 ± 1.59† |
| $SiO_{2(s,\ cristobalite,\ 25\ °C)} \rightarrow SiO_{2(sln,\ cristobalite,\ 804\ °C)}$ | $\Delta H_5$ ($SiO_2$) = 48.55 ± 1.54† |
| $Al_2O_{3(s,\ corrundum,\ 25\ °C)} \rightarrow Al_2O_{3(sln,\ 804\ °C)}$ | $\Delta H_6$ ($Al_2O_3$) = 109.00 ± 1.60† |
| $nH_2O_{(s,\ 25\ °C)} \rightarrow nH_2O_{(g,\ 804\ °C)}$ | $\Delta H_7$ ($H_2O$) = 73.22 ± 0.72† |
| Calculation of $\Delta H_{f,ox}$ at 25 °C (kJ/mol) | |
| $[(½)\{xK_2O + yNa_2O + zCs_2O + mAl_2O_3\} + SiO_2 + nH_2O]_{(s,\ 25\ °C)} \rightarrow K_{(0.5x)}Na_{(0.5y)}Cs_{(0.5z)}Al_{(0.5m)}Si_{(1.0)}O_{(q(0.5(x+y+z+m)+Si)}.nH_2O]_{(s,\ 25\ °C)}$ | |
| $\Delta H_8 = ½(x)\Delta H_2 + ½(y)\Delta H_3 + ½(z)\Delta H_4 + \Delta H_5 + ½(m)\Delta H_6 + n\Delta H_7 - \Delta H_1$ | |

s = solid; sln = solution; $\Delta H_5 = \Delta H_{(T,\ 25–804\ °C)}$ = heat content enthalpy over the temperature range 25–804 °C. †Measured or computed data from this work.

### 4.6. Formation enthalpies

Demonstrated in the formation enthalpies from the oxides, the nascent and cation-satureted zeolites are thermodynamically stable relative to their condensed phase oxide reaction components. The $\Delta H_{f,ox}$ general trend observed for the nascent zeolites, from greater to lesser stability, is −142.42 ± 6.78 (NaX) > −97.56 ± 5.82 (NaY) > −33.53 ± 5.25 (HY 2.6) > −22.26 ± 4.78 (HY 15) > −5.01 ± 4.47 (HY 40) in units kJ/mol. For the $Na^+$- and $Cs^+$-saturated zeolites, respectively, the trend is −156.47 ± 7.42 ($Na^+$-NaX) > −77.90 ± 6.31 ($Na^+$-NaY) > −37.50 ± 5.24 ($Na^+$-HY) and −272.02 ± 8.01 ($Cs^+$-NaX) > −104.01 ± 6.81 ($Cs^+$-NaY) > −37.94 ± 5.01 ($Cs^+$-HY) in units kJ/mol. Formation enthalpy from the oxides, $\Delta H_{f,ox}$, against Si/Al located a stability relationship that is *inversely related*. With *increasing* Si/Al, condensed phase *stability decreases for these zeolites*. As shown on Fig. 7, we observe a deep decrease of stability up to Si/Al equal 3.3, and then a plateau of enthalpy of formation. This means that FAU-Y is less stable than FAU-X. Of interest, the formation enthalpy against Si/Al for the HY series is linear with a constant enthalpy that tracks with its NaY parent phase. However, the HY series trend is independent of NaY by an order of magnitude less stability. Typically, HY is produced from NaY by $H^+$-exchange and calcination, which would affect the microstructure relative to the original NaY and subsequently produced the dramatic decrease in HY formation enthalpy. Changes to the microstructure could include pore size, hydration level, and exchange site accessibility.

The trend holds for both the hydrous as well as anhydrous forms of the nascent zeolites and their cation-exchanged products indicating a strong dependency of stability on Si/Al ratio. Certainly, water content has a contribution due to its stabilizing influence in these mineral phases as well. Likewise, cation substitution is strongly thermodynamically stabilizing. It is evident that cation-exchanged zeolite stability tends to increase with incorporation of *alkali of decreasing electronegativity (traveling further down the Group-I cations)*.

An increase in thermodynamic stability occurs on the incorporation of $Na^+$ into the zeolite, without $Cs^+$ in structure, as shown on Fig. 8a. This is closely linked to the Si/Al ratio: increasing guest ions in the structure (so Al content) leads to a decrease of Si/Al ratio, and then an increase of the stability (see **Figure**). Addition of $Cs^+$ in the structure leads to an increase of the stability, as reported on Fig. 8a (point in red).

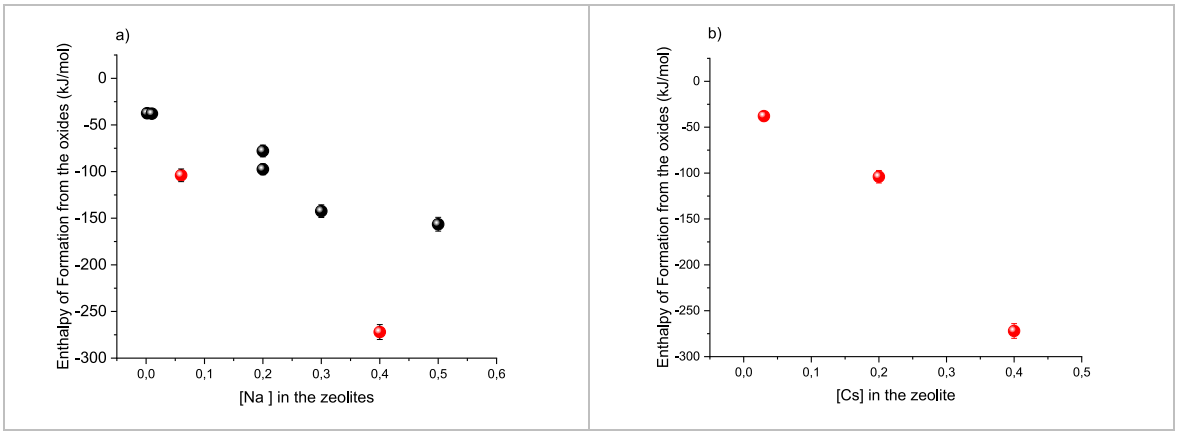


**Fig. 8.** Enthalpy of formation from the binary oxides at 25 °C is plotted against the exchanged cation content a) for the $Na^+$ saturated zeolites (point in red corresponding to $Cs^+$ exchanged zeolite) and b) for the $Cs^+$ saturated zeolites.

Moreover as shown on Fig. 8b, an increase of $Cs^+$ in the structure increases the stability of the zeolite, whatever the amount of $Na^+$. This means that $Cs^+$ stabilizes the zeolitic structure.

In general, the lower stability phase tends to be more reactive (e.g., catalysts, ion conductors). *NaY* (NaY < NaX) *should follow this trend and react to a greater extent incorporating Cs* $^+$ *than NaX*. Typically, $Cs^+$ incorporation is stabilizing. In additional porous phases previously studied the general trend is that the lower stability phase may gain greater stability through increased $Cs^+$ cation adsorption. These points may lead one to hypothesize that as the lower stability phase may find increased thermodynamic stability with cation incorporation into the structure so too this should be expected to result in increased adsorption capacity. That is assuming that there is structural access to the mineral phase. The $Cs^+$-adsorption isotherms should then demonstrate increased uptake by $Na^+$-NaY relative to the other sodium-substituted zeolites.

### 4.7. Adsorption isotherms

$Cs^+$ adsorption isotherms for the $Na^+$-saturated zeolites in pH 5, are given in Fig. 9. Based on these experimental results, the Langmuir model, which is described by Eq. (4), has been applied.

$$\frac{C_e}{Q_e} = \frac{1}{q_m K_L} + \frac{C_e}{Q_m} \qquad \text{Eq. 6}$$

Here, $C_e$ is equal to the equilibrium adsorption concentration ($mg{\cdot}L^{-1}$), $Q_e$ (equilibrium, $mg{\cdot}g^{-1}$) represents the amount of $Cs^+$ adsorbed at the equilibrium, the maximum adsorption capacity in $mg{\cdot}g^{-1}$ is represented by $Q_m$, and the Langmuir constant in L/mg is denoted, $K_L$. The latter, $K_L$, is related to the adsorbate's affinity to the adsorbent.

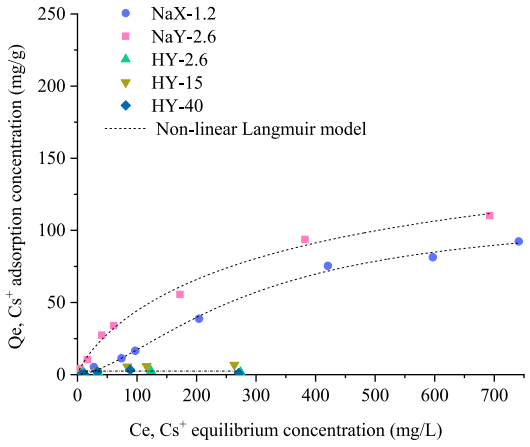


**Fig. 9.** Cs adsorption isotherms of the commercial NaX, NaY and acid zeolites.

To calculate the maximum adsorption capacities, the adsorption isotherms have been fitted with Langmuir models. This model can fit correctly the data from the $Cs^+$ adsorption isotherm of the $Na^+$- NaX and $Na^+$-NaY zeolite with a high $R^2$ values (≥0.99) but this value decreases to 0.62 for acidic zeolite, making this model unsuitable. The Langmuir model is most used for the adsorption in liquid media and based on different conjectures as the adsorption occurs on the homogeneous sites in adsorbent with equivalent energy. Indeed, $Cs^+$ ions can be adsorbed in the zeolite structure by ionic exchange mechanism with $Na^+$. This gives a Langmuir maximum $Cs^+$ adsorption capacity for $Na^+$-NaX and $Na^+$-NaY equal to 91 mg $g^{-1}$ and 113 mg $g^{-1}$ and corresponding to 1.4 mmol $g^{-1}$ and 1.7 mmol $g^{-1}$, respectively.

These results, raised intriguing questions, especially when considering the number of available sodium sites for ion exchange. To delve further into these disparities, theoretical calculations were performed. Considering the chemical formulas of the two faujasite zeolites, namely X ($Na_{20}Al_{20}Si_{28}O_{96}$) and Y ($Na_{14}Al_{14}Si_{34}O_{96}$), with sodium atom distributions in X as (8 in site II, 4 in site III, 6 in site I′, and 2 in site I), and in Y as (8 in site II, 4 in site I′, and 2 in site I).

The calculation reveal that the experimental data of 113 mg/g for NaY corresponds to the exchange of approximately 2.6 Cs atoms from the 14 available sodium atoms. Similarly, the 91 mg/g observed for NaX equates to roughly 2.3 Cs atoms exchanged from the 20 available sodium atoms. Remarkably, the Cs atoms exchanged with Na atoms remain almost identical in number despite the disparity in adsorption capacities for Cs in X and Y.

Further investigation into these structures reveals that, theoretically, the maximum exchange capacity for NaY, involving all 14 sodium sites, could yield a Cs loading of 583 mg/g, whereas for NaX, which has 20 sodium sites, the potential Cs loading could reach 800 mg/g.

When considering the accessibility of ion exchange sites within the faujasite framework, it becomes evident that the distribution of sodium atoms plays a critical role in understanding the observed disparities in Cs adsorption. In the case of NaY, a zeolite with 8 Na ions situated at site II, it is apparent that the exchange of these accessible sites could theoretically yield a Cs loading of 333 mg/g. Conversely, NaX exhibits a similar distribution of 8 Na ions at site II, but with 4 supplementary Na ions located at site III'. This configuration offers the potential for the exchange of 480 mg/g of Cs, underscoring the significance of site accessibility in explaining the higher Cs adsorption observed in NaX. Now, when we scrutinize our experimental findings of Cs adsorption capacity,

namely 113 mg/g for NaY and 91 mg/g for NaX, it becomes evident that the observed values fall significantly below the theoretical adsorption capacities derived from our calculations. This discrepancy underscores the complexity of ion exchange processes within zeolite frameworks, revealing that there are additional factors at play that hinder the complete realization of their ion exchange potential.

An in-depth exploration of the disparities in Cs adsorption across these two zeolites uncovers several pivotal elements that influence their behavior: this result cannot be explained by the amount of guest ion in the zeolitic structure that is higher for NaX than NaY (see Table 1). However, this result can be explained thanks to the previous results.

- Thermodynamics studies show that NaY has higher unstability and reacts to greater amount of Cs $^{+}$ as explained in the previous paragraph.
- Structural XRD studies show that $Na^+$ in NaX are mostly in site I and site I' (not easily exchangeable). Likewise, although exchange of NaY to form $Na^+$-NaY resulted in some loss of crystallinity and thus of phase stability. This was more than compensated for on Cs-exchange resulting in significant phase stability increase in the $Cs^+$-NaY product.
- DFT predict a smaller accessible pore volume in NaX than NaY.

The three acidic zeolites provide a weaker Langmuir maximum $Cs^+$ adsorption capacity $<10$ mg $g^{-1}$. Indeed, as discussed previously, these zeolites are strongly pH-dependent with a $Cs^+$ sorption being lower at pH 5 than at pH 6 or 7. In this study, the lower sorption at pH 5 would result from the grown dissolution of a part of the zeolite in acidic conditions and the increase concentration of $H^+$ originated from the dissociation of water. A dealumination progress of zeolite at acidic pH and the presence of proton as a competitive ion decrease the adsorption rate related to the $Cs^+$ adsorption selectivity of zeolite. The $H^+$ selective adsorption of the zeolites differs from each other and more the cation sites decreases with the pH and higher is the $H^+$ affinity. In addition, the acidic zeolite presents Al–OH–Si covalent bonds in their structural framework, which are stronger than the electrostatic force between $Na^+$ and the negative charge from Al–O–Si linkage in NaX and NaY. As such, the exchange mechanism between $H^+$ and $Na^+$ increases in difficulty, which explains the low $Cs^+$ adsorption rate for the three acidic zeolites.

## 5. Conclusions

Empirical and computational techniques were applied in this study to investigate the effects of cation substitution on the structure and stability of Faujasite zeolites, and a correlation to Cs-adsorption efficiency.

While the guest ion number in NaX structure is greater than that of NaY structure, a lower sorption capacity is obtained for NaX structure. This can be explain by a rate of occupancy of un-exchangeable sites (Site I and site I') higher for NaX than for NaY. DFT calculations showed that site III exchange was more favorable than site II exchange in NaX and the relatively least favorable exchange was at site II in NaY. Moreover, in case of $Cs^+$ exchanged NaY, Cs + cations occupy also site III, which is not the case of NaX.

$Cs^+$ exchanged zeolite increases this amount of guest ions for NaX, and has poor effect for NaY. This leads also to a decrease of the microporosity of the zeolite by the insertion of Cs into the cell. The better incorporation of $Cs^+$ inside the structure is in agreement with thermodynamics data showing a lower stabilization of $Cs^+$ exchanged NaY ($-26$ kJ/mol between Na + -NaY and Cs + -NaY) than Cs + exchange NaX ($-116$ kJ/mol between $Na^+$-NaX and $Cs^+$-NaY). Additionally, increasing Si/Al ratio decreases the stability of Faujasite structures, meaning that NaY zeolite is less stable than NaX.

Notably, the Na–Y structure was found to be a crucial factor in controlling $Cs^+$ exchange in Fau-Y, leading to increased reactivity and isothermal exchange compared to Na-X or Na-HY. The adsorption of $Cs^+$ on zeolite faujasite in aqueous media shows a strong dependence of pH. NaX with the lower Si/Al ratio and potentially the highest negative charge has a higher selectivity for $H^+$ instead of $Cs^+$ as compared to NaY. This ion competition is emphasized with the decrease of pH. In addition, under acidic conditions, a dissolution of a part of the zeolite occurs during the experiments contributing to a lower Cs + adsorption rate. The Cs $^{+}$ adsorption selectivity sequence of the zeolite followed: NaY $>$ NaX $>$ HY.

In summary, the interplay among stability, structure, surface chemistry, porosity, and energetics of the zeolite landscape are demonstrated here as powerful drivers for $Cs^+$ uptake efficiency in zeolites. Collective interpretation of all of these contributing factors appears to be crucial as any one of these variables taken without consideration of the others may be misleading. Overall, the findings provide new insights into Faujasite $Cs^+$ exchange and demonstrate the importance of considering both structure and thermodynamics when designing and optimizing Faujasite-based materials. The complexities observed in the HY zeolites also highlight the need for further research to improve understanding of the changes to the parent Fau-Y structure that diminished the function and stability of Fau-HY.

## CRediT authorship contribution statement

**Nancy Birkner:** Writing – original draft. **Vanessa Proust:** Writing – original draft, Conceptualization. **Joe Schaeperkoetter:** Formal analysis. **An T. Ta:** Formal analysis. **Alban Gossard:** Writing – review & editing. **Ayoub Daouli:** Writing – review & editing. **Michael Badawi:** Writing – review & editing, Conceptualization. **Nakeshma Cassell:** Formal analysis. **Scott Misture:** Writing – review & editing. **Simon R. Phillpot:** Writing – review & editing. **Hans-Conrad zur Loye:** Writing – review & editing, Supervision, Conceptualization. **Kyle S. Brinkman:** Writing – review & editing. **Agnès Grandjean:** Writing – review & editing, Validation, Supervision, Conceptualization.

## Declaration of competing interest

The authors declare that they have no known competing financial interests or personal relationships that could have appeared to influence the work reported in this paper.

## Data availability

No data was used for the research described in the article.

## Acknowledgements

This work was supported as part of the Center for Hierarchical Waste Form Materials, an Energy Frontier Research Center funded by the U.S. Department of Energy, Office of Science, Basic Energy Sciences under Award No. DE-SC0016574. This work was also supported the CEA energy division's cross-cutting basic research program (RTA Program). We thank Audrey Hertz, Virginie Fremy and Benoit Meilleray for their help with the sample analysis.

## Appendix A. Supplementary data

Supplementary data to this article can be found online at https://doi.org/10.1016/j.micromeso.2024.113110.

## References

[1] C.E.W. Topping, M.K.I.L. Abella, M.E. Berkowitz, M.R. Molina, I. Nikolić-Hughes, E.W. Hughes, M.A. Ruderman, *In situ* measurement of cesium-137 contamination in fruits from the northern Marshall Islands, Proc. Natl. Acad. Sci. U. S. A. 116 (2019) 31.

[2] M. Hori, T. Saito, K. Shozugawa, Source evaluation of 137Cs in foodstuffs based on trace 134Cs radioactivity measurements following the Fukushima nuclear accident, Sci. Rep. 8 (2018) 1.
[3] Federal radiation council, Report No. 7: Background Material for the Development of Radiation Protection Standards: Protective Action Guides for Strontium-89, Strontium 90 and Cesium-137, US EPA, 1965.
[4] K.-M. Wai, D. Krstic, D. Nikezic, T.-H. Lin, P.K.N. Yu, External cesium-137 doses to humans from soil influenced by the Fukushima and Chernobyl nuclear power plants accidents: a comparative study, Sci. Rep. 13 (2020) 10, 1.
[5] Christer Persson, et al., The Chernobyl accident: a meteorological analysis of how radionuclides reached and were deposited in Sweden, Ambio 16 (1987) JSTOR.
[6] D.A. Wheeler, Atmospheric dispersal and deposition of radioactive material from Chernobyl, Atmos. Environ. 22 (1988) 5.
[7] M. Aoyama, Long-range transport of radiocaesium derived from global fallout and the Fukushima accident in the pacific ocean since 1953 through 2017-Part I: source term and surface transport, J. Radioanal. Nucl. Chem. (2018) 318.
[8] M. Aoyama, Y. Hamajima, Mikael Hult, M. Uematsu, E. Oka, D. Tsumune, Y. Kumamoto, 134Cs and 137Cs in the north pacific ocean derived from the march 2011 TEPCO Fukushima Dai-Ichi nuclear power plant accident, Japan. Part One: surface pathway and vertical distributions, J. Oceanogr. (2015) 72.
[9] M. Aoyama, M. Kajino, T.Y. Tanaka, T. Sekiyama, T. Tsubono, Y. Hamajima, T. Gamo, Cs and 137 Cs in the north pacific ocean derived from the march 2011 TEPCO Fukushima Dai-Ichi nuclear power plant accident, Japan. Part Two: estimation of 134 Cs and 137 Cs inventories in the north pacific ocean, J. Oceanogr. (2016) 72.
[10] C. Persson, H. Rodhe, L.-E. De Geer, The Chernobyl accident: a meteorological analysis of how radionuclides reached and were deposited in Sweden, Ambio (1987) 16.
[11] M. Jiménez-Reyes, et al., Radioactive waste treatments by using zeolites, A short review, J. Environ. Radioact. (2021) 233.
[12] Y. Zhu, et al., Advances in immobilization of radionuclide wastes by alkali activated, Cem. Con. Comp. (2022) 126.
[13] A.I. Orlova, M.I. Ojovan, Ceramic mineral waste-forms for nuclear waste immobilization, Match (2019) 12.
[14] M. Arbel-Haddad, Y. Harnik, Y. Schlosser, et al., Cesium immobilization in metakaolin-based geopolymers elucidated by 133Cs solid state NMR spectroscopy, J. Nucl. Mater. (2022) 562.
[15] P. Bosch, et al., Safe trapping of Cs in heat-treated zeolite matrices, J. Nucl. Mater. (2003) 324.
[16] L. Heyao, T. Lizhi, S. Minhua, C. Diyun, S. Gang, Z. Ying, The latest research trends in the removal of cesium from radioactive wastewater: a review based on data-driven and visual analysis, Sci. Total Environ. (2023) 869.
[17] C. Cabaud, et al., "Linking the multiscale porous structure of hexacyanoferrate-loaded silica monoliths to their hydrodynamic and cesium sorption properties", Se Pu (2019) 229.
[18] H. Mimura, N. Sato, A. Kirishima, «Selective separation and solidification of radioactive nuclides by zeolites", J. Ion Exchange 22 (2011).
[19] G. Martra, R. Ocule, L. Marchese, G. Centi, S. Coluccia, Alkali and alkaline-earth exchanged faujasites: strength of Lewis base and acid centres and cation site occupancy in Na- and BaY and Na- and BaX zeolites, Catal. Today 73 (2002).
[20] C. Liu, I. Tranca, R.A. Van Santen, E.J.M. Hensen, E.A. Pidko, Scaling relations for acidity and reactivity of zeolites, J. Phys. Chem. C (2017) 121.
[21] X. Du, H. Zhang, X. Li, Z. Tan, H. Liu, X. Gao, Cation location and migration in lanthanum-exchanged NaY zeolite, Chin. J. Catal. (2013) 34.
[22] A. Zecchina, R. Buzzoni, S. Bordiga, F. Geobaldo, D. Scarano, G. Ricchiardi, G. Spoto, Host- guest interactions in zeolite cavities, Stud. Surf. Sci. Catal. 97 (1995).
[23] G. Li, E.A. Pidko, The nature and catalytic function of cation sites in zeolites: a computational perspective, ChemCatChem (2019) 11.
[24] S. Uchida, Frontiers and progress in cation-uptake and exchange chemistry of polyoxometalate-based compounds, Chem. Sci. 10 (2019).
[25] M. Jiménez-Reyes, P.T. Almazán-Sánchez, M. Solache-Ríos, Radioactive waste treatments by using zeolites. A short review, J. Environ. Radioact. (2021) 233.
[26] A.E. Osmanlioglu, Treatment of radioactive liquid waste by sorption on natural zeolite in Turkey, J. Hazard Mater. (2006) 137.
[27] A. Navrotsky, Thermochemistry of New, Technologically Important Inorganic Materials, Cambridge University Press, 1997. MRS bulletin.
[28] A. Navrotsky, "Progress and new directions in high temperature calorimetry revisited", Phys. Chem. Miner. 24 (1997).
[29] A. Navrotsky, Progress and new directions in calorimetry: a 2014 perspectiv", J. Am. Ceram. Soc. (2014) 97.
[30] D. Gorman-Lewis, L. Mazeina, J.B. Fein, J.E.S. Szymanowski, P.C. Burns, A. Navrotsky, " thermodynamic properties of soddyite from solubility and calorimetry measurements", J. Chem. Thermodyn. (2007) 39.
[31] G. Kresse, J. Hafner, Ab Initio molecular dynamics for liquid metals, Phys. Rev. B 47 (1993).
[32] G. Kresse, J. Furthmüller, "Efficient iterative schemes for Ab Initio total-energy calculations using a plane-wave basis set", Phys. Rev. B Condens. Matter (1996) 54.
[33] G. Kresse, Furthmüller, "J. Efficiency of Ab-Initio total energy calculations for metals and semiconductors using a plane-wave basis set.", Comput. Mater. Sci. 6 (1996).
[34] J.P. Perdew, K. Burke, M. Ernzerhof, "Generalized gradient approximation made simple", Phys. Rev. Lett. (1996) 77.
[35] P.E. Blochl, "Projector augmented-wave method", Phys. Rev. B 50 (1994).
[36] G. Kresse, D. Joubert, From Ultrasoft pseudopotentials to the projector augmented-wave method, Phys. Rev. B (1999) 59.
[37] H.J. Monkhorst, J.D. Pack, Special points for brillouin-zone integrations, Phys. Rev. B 13 (1976).
[38] S. Grimme, Semiempirical GGA-type density functional constructed with a long-range dispersion correction, J. Comput. Chem. (2006) 27.
[39] L. Sellaoui, E.P. Hessou, M. Badawi, M.S. Netto, G.L. Dotto, L.F.O. Silva, F. Tielens, J. Ifthikar, A. Bonilla-Petriciolet, Z. Chen, Trapping of Ag+, Cu2+, and Co2+ by faujasite zeolite Y: new interpretations of the adsorption mechanism via DFT and statistical modeling investigation, Chem. Eng. J. 420 (2021).
[40] M. Chebbi, S. Chibani, J.F. Paul, L. Cantrel, M. Badawi, Evaluation of volatile iodine trapping in presence of contaminants: a periodic DFT study on cation exchanged-faujasite, Microporous Mesoporous Mater. 239 (2017).
[41] T. Frising, P. Leflaive, Extraframework cation distributions in X and Y faujasite zeolites: a review, Microporous Mesoporous Mater. (2008) 114.
[42] T.F. Willems, C.H. Rycroft, M. Kazi, J.C. Meza, M. Haranczyk, Algorithms and tools for high-throughput geometry-based analysis of crystalline porous materials, Microporous Mesoporous Mater. (2012) 149.
[43] M.W. Munthali, et al., Cs+ and Sr2+ adsorption selectivity of zeolites in relation to radioactive decontamination, Journal of Asian Ceramic Societies 3 (2015).
[44] M.W. Munthali, M.A. Elsheikh, E. Johan, N. Matsue, Proton adsorption selectivity of zeolites in aqueous media: effect of Si/Al ratio of zeolites, Molecules 19 (2014).
[45] E.J. García, J.A. Pérez-Pellitero, G.D. Pirngruber, C. Jallut, M. Palomino, F. Rey, S. Valencia, Tuning the adsorption properties of zeolites as adsorbents for CO2 separation: best compromise between the working capacity and selectivity, Ind. Eng. Chem. Res. (2014) 53.
[46] J. Sebastian, S. Pillai Renjith, S.A. Peter, R.V. Jasra, Sorption of $N_2$, $O_2$, and Ar in Mn(II)-Exchanged zeolites A and X using volumetric measurements and grand canonical Monte Carlo simulation, Ind. Eng. Chem. Res. 46 (2007).
[47] D. Bonenfant, M. Kharoune, P. Niquette, M. Mimeault, R. Hausler, Advances in principal factors influencing carbon dioxide adsorption on zeolites, Sci. Technol. Adv. Mater. 9 (2008).
[48] Y. Lee, S.W. Carr, J.B. Parise, Phase transition upon $K^+$ ion exchange into Na-low silica X: combined NMR and synchrotron X-ray powder diffraction study, Chem. Mater. 10 (1998).
[49] L. Zhu, K. Seff, Cation crowding in zeolites. Reinvestigation of the crystal structure of dehydrated potassium-exchanged zeolite X, J. Phys. Chem. B (2000) 104.
[50] I.K. Butikova, Y.F. Shepelev, Y.I. Smolin, Crystal structure of CsNaX-zeolite in hydrated and dehydrated forms, Kristallografiya (1989) 34.
[51] R. Arletti, et al., Evidence for the formation of stable CO2 hydrates in zeolite Na Y: structural characterization by synchrotron X-ray powder diffraction, Microporous Mesoporous Mater. (2016) 228.
[52] J.D. Rimer, O. Trofymluk, A. Navrotsky, R.F. Lobo, Kinetic and thermodynamic studies of silica nanoparticle dissolution, Chem. Mater. 19 (2007).
[53] B. Roy N, A. Navrotsky, Thermochemistry of charge-coupled substitutions in silicate glasses: the systems ml/n N+A1O 2-SiOz, J. Am. Soc. 67 (1984).